

Unified Regularization of 2D Singular Integrals for Axisymmetric Galerkin BEM in Eddy-Current Evaluation

Yao Luo^{a,*}

^a*School of Electrical Engineering and Automation, Wuhan University, Wuhan 430072, China*

Abstract

This paper presents an axisymmetric Galerkin boundary element method (BEM) for modeling eddy-current interactions between excitation coils and conductive objects. The formulation derives boundary integral equations from the Stratton–Chu representation for the azimuthal component of the vector potential in both air and conductive regions. The central contribution is a unified regularization framework for the two-dimensional (2D) singular integrals arising in Galerkin BEM. This framework handles both logarithmic and Cauchy singularities through a common set of integral transformations, eliminating the need for case-by-case analytical singularity extraction and enabling straightforward numerical quadrature. The regularization and quadrature stability are proved and verified numerically. The method is validated on several representative axisymmetric geometries, including cylindrical, conical, and spherical shells. Numerical experiments demonstrate consistently high accuracy and computational efficiency across broad frequency ranges and coil lift-off distances. The results confirm that the proposed axisymmetric Galerkin BEM, combined with the integral transformation technique, provides a robust and efficient framework for axisymmetric eddy-current non-destructive evaluation.

Keywords: eddy-current testing, Galerkin boundary element method, axisymmetric model, singular integral, coordinate transformation

*Corresponding author. E-mail: sturmjungling@gmail.com. Currently visiting researcher at the Department of Electronics, Information and Bioengineering (DEIB), Politecnico di Milano.

1. Introduction

Eddy-current nondestructive evaluation (EC-NDE) is widely used for conductivity measurement, flaw detection, thickness estimation, and material sorting [1, 2]. Many important inspection scenarios, such as heat-exchanger tubes, steam-generator tubing, cylindrical shells, and rod-type components, exhibit axial symmetry. In such cases, boundary-integral formulations are especially attractive because only the one-dimensional meridional curve needs to be discretized, whereas finite-element models require meshing of the entire 2D cross-section.

Most existing axisymmetric BEM models employ collocation formulations [3]. Despite the conceptual simplicity of this framework, several computational challenges arise in practice. While the axisymmetric Laplace kernel admits closed-form expressions in terms of elliptic integrals, the axisymmetric Helmholtz kernel does not [4]. Consequently, several studies have developed ad hoc numerical techniques to approximate the Helmholtz kernel [5, 6]. Moreover, even for the axisymmetric Laplace kernel, the closed-form expressions for singular integrals become intricate for constant elements, and their extension to higher-order elements dramatically increases the algebraic complexity [7]. These same difficulties arise in the analytical extraction of singularities from the Helmholtz kernel, since the singular part corresponds precisely to the Laplace kernel.

The Galerkin boundary element method (Galerkin BEM) offers a natural alternative that is particularly well-suited for higher-order accuracy, as its variational foundation provides stable projection onto the trial space and guarantees quasi-optimal error bounds [8]. However, its application to axisymmetric eddy-current analysis has remained limited. The primary obstacle is numerical rather than conceptual: Galerkin BEM requires reliable evaluation of double integrals involving products of basis functions and singular kernels. Classical analytical extraction techniques become increasingly impractical, as their complexity depends on both the element order and kernel type, escalating rapidly for higher-order elements.

The present work addresses this gap by introducing a coordinate transformation tailored to 2D Galerkin BEM. This construction yields smooth integrands in all relevant configurations, enabling accurate Gauss-Legendre (GL) quadrature without the analytical extraction linked to the kernel or element

order. The resulting scheme handles logarithmic and Cauchy singularities in a unified manner, rendering a fully general axisymmetric Galerkin BEM practical for eddy-current modeling. The regularization depends solely on the local geometry of the two interacting boundary segments, independent of any global geometric assumptions. Consequently, although the present work focuses on axisymmetric eddy-current problems, the methodology provides a unified treatment of singular integrals applicable to any 2D Galerkin BEM. Its potential applications thus extend well beyond rotationally symmetric configurations.

The proposed method is validated against reference finite-element solutions for three geometries of increasing complexity. Linear elements demonstrate consistent second-order convergence with mesh refinement, while quadratic isoparametric elements achieve relative errors of 10^{-5} even on the coarsest discretizations. These results establish that Galerkin BEM combined with the proposed regularization delivers exceptional accuracy, geometric versatility, and computational efficiency for axisymmetric eddy-current problems.

2. Boundary integral equations for the axisymmetric vector potential

2.1. Boundary integral equations derived from the Stratton-Chu formula

Consider an eddy-current coil carrying current with amplitude I and angular frequency ω , placed near a conductive object with conductivity σ and permeability μ . Neglecting the displacement current, the governing equations for the vector potential \mathbf{A} are

$$\nabla^2 \mathbf{A} = -\mu \mathbf{J}^{(e)} \quad (1)$$

in the air, where $\mathbf{J}^{(e)}$ is the current density of the source, and

$$\nabla^2 \mathbf{A} + k^2 \mathbf{A} = 0 \quad (2)$$

in the conductive domain, where

$$k^2 = -i\omega\mu\sigma \quad (3)$$

Here k denotes the complex wavenumber with $\Re(k) > 0$. Boundary integral equations (BIE) will be derived with the vector version of Green's second identity, i.e. the Stratton-Chu formula [9]:

$$\int_{\Omega} (G \nabla^2 \mathbf{A} - \mathbf{A} \nabla_{\mathbf{y}}^2 G) d\Omega = \int_{\Gamma} \left[(\nabla \cdot \mathbf{A}) G \mathbf{n} - (\mathbf{n} \cdot \mathbf{A}) \nabla_{\mathbf{y}} G - \mathbf{n} \times (\nabla \times \mathbf{A}) G - (\mathbf{n} \times \mathbf{A}) \times \nabla_{\mathbf{y}} G \right] d\Gamma \quad (4)$$

for the free space, where Γ denotes the boundary of the region Ω , \mathbf{n} is the unit normal vector pointing into the free space, and G is the fundamental solution (FS)

$$G(\mathbf{x}, \mathbf{y}) = \frac{1}{4\pi|\mathbf{x} - \mathbf{y}|} \quad (5)$$

satisfying

$$\nabla_{\mathbf{y}}^2 G(\mathbf{x}, \mathbf{y}) = -\delta(\mathbf{x} - \mathbf{y}) \quad (6)$$

where \mathbf{x} and \mathbf{y} are the field and source points, respectively, δ is the Dirac delta function, and $|\mathbf{x} - \mathbf{y}|$ is the distance between them.

When \mathbf{x} is on the boundary Γ , a BIE can be obtained from equations (1), (4), and (6) by a limit procedure:

$$\frac{\Omega(\mathbf{x})}{4\pi} \mathbf{A}(\mathbf{x}) + \int_{\Gamma} \left[(\mathbf{n} \cdot \mathbf{A}) \nabla_{\mathbf{y}} G(\mathbf{x}, \mathbf{y}) + \mathbf{n} \times (\nabla \times \mathbf{A}) G(\mathbf{x}, \mathbf{y}) + (\mathbf{n} \times \mathbf{A}) \times \nabla_{\mathbf{y}} G(\mathbf{x}, \mathbf{y}) \right] d\Gamma_{\mathbf{y}} = \mathbf{A}^{(e)}(\mathbf{x}), \quad (7)$$

where $\Omega(\mathbf{x})$ is the solid angle at point \mathbf{x} , and $\mathbf{A}^{(e)}(\mathbf{x})$ is the source vector potential at the same point:

$$\mathbf{A}^{(e)}(\mathbf{x}) = \mu_0 \int_{\Omega} \mathbf{J}^{(e)}(\mathbf{y}) G(\mathbf{x}, \mathbf{y}) d\Omega_{\mathbf{y}}. \quad (8)$$

In equation (7), the Coulomb gauge $\nabla \cdot \mathbf{A} = 0$ is assumed. Applying equation (2) together with the electrodynamic counterpart of (4) yields

$$\begin{aligned} & \int_{\Omega} (G_k(\nabla^2 \mathbf{A} + k^2 \mathbf{A}) - \mathbf{A}(\nabla^2 G_k + k^2 G_k)) d\Omega \\ &= \int_{\Gamma} \left[\mathbf{n}_{\mathbf{y}} (\nabla \cdot \mathbf{A}) G_k(\mathbf{x}, \mathbf{y}) - (\mathbf{n}_{\mathbf{y}} \cdot \mathbf{A}) \nabla_{\mathbf{y}} G_k(\mathbf{x}, \mathbf{y}) - \mathbf{n}_{\mathbf{y}} \times (\nabla \times \mathbf{A}) G_k(\mathbf{x}, \mathbf{y}) - (\mathbf{n}_{\mathbf{y}} \times \mathbf{A}) \times \nabla_{\mathbf{y}} G_k(\mathbf{x}, \mathbf{y}) \right] d\Gamma_{\mathbf{y}}, \end{aligned} \quad (9)$$

where $G_k = \exp(-ik|\mathbf{x} - \mathbf{y}|)/(4\pi|\mathbf{x} - \mathbf{y}|)$ denotes the FS satisfying

$$\nabla_{\mathbf{y}}^2 G_k + k^2 G_k = -\delta(\mathbf{x} - \mathbf{y}). \quad (10)$$

Consequently, the BIE for the conductive region becomes

$$\begin{aligned} \frac{\Omega(\mathbf{x})}{4\pi} \mathbf{A}(\mathbf{x}) + \int_{\Gamma} \left[(\mathbf{n} \cdot \mathbf{A}) \nabla_{\mathbf{y}} G_k(\mathbf{x}, \mathbf{y}) + \mathbf{n} \times (\nabla \times \mathbf{A}) G_k(\mathbf{x}, \mathbf{y}) \right. \\ \left. + (\mathbf{n} \times \mathbf{A}) \times \nabla_{\mathbf{y}} G_k(\mathbf{x}, \mathbf{y}) \right] d\Gamma_{\mathbf{y}} = 0. \end{aligned} \quad (11)$$

For an axisymmetric problem, the vector potential \mathbf{A} possesses only an azimuthal component in cylindrical coordinates (r, φ, z) . Consequently, equations (7) and (11) reduce to the axisymmetric BEM formulation:

$$c(\mathbf{x}) u^{(1)}(\mathbf{x}) + \int_{\gamma} [\mathcal{G}(\mathbf{x}, \mathbf{y}) q^{(1)}(\mathbf{y}) - u^{(1)}(\mathbf{y}) \partial_{\mathbf{n}_y} \mathcal{G}(\mathbf{x}, \mathbf{y})] r_{\mathbf{y}} ds_{\mathbf{y}} = u^{(e)}(\mathbf{x}) \quad (12)$$

and

$$(1 - c(\mathbf{x})) u^{(2)}(\mathbf{x}) + \int_{\gamma} [u^{(2)}(\mathbf{y}) \partial_{\mathbf{n}_y} \mathcal{G}_k(\mathbf{x}, \mathbf{y}) - \mathcal{G}_k(\mathbf{x}, \mathbf{y}) q^{(2)}(\mathbf{y})] r_{\mathbf{y}} ds_{\mathbf{y}} = 0, \quad (13)$$

where the superscripts (1) and (2) denote the non-conductive and conductive regions, respectively, γ denotes the meridional curve, and

$$\begin{aligned} u(\mathbf{x}) &:= A_{\varphi}(\mathbf{x})|_{\gamma}, \\ q(\mathbf{x}) &:= \partial_{\mathbf{n}} A_{\varphi}(\mathbf{x})|_{\gamma} \end{aligned} \quad (14)$$

represent the azimuthal component and its normal derivative on the boundary, respectively. The normal derivative is evaluated as

$$\frac{\partial}{\partial n} \equiv n_r \frac{\partial}{\partial r} + n_z \frac{\partial}{\partial z} \quad (15)$$

In equations (12) and (13), \mathcal{G} and \mathcal{G}_k denote the axisymmetric Laplace and Helmholtz kernels, respectively, whose explicit expressions are provided in Appendix C.

2.2. Galerkin BIE and discretization

Multiplying both sides of equation (12) by the test function $\phi_i(\mathbf{x})$ and integrating with respect to \mathbf{x} over the boundary γ yields the Galerkin BIE:

$$\begin{aligned} & \int_{\gamma} \phi_i(\mathbf{x}) \{ c(\mathbf{x}) u^{(1)}(\mathbf{x}) \\ & \quad + \int_{\gamma} [\mathcal{G}(\mathbf{x}, \mathbf{y}) q^{(1)}(\mathbf{y}) - u^{(1)}(\mathbf{y}) \partial_{\mathbf{n}_y} \mathcal{G}(\mathbf{x}, \mathbf{y})] r_{\mathbf{y}} d\mathbf{s}_{\mathbf{y}} \\ & \quad - u^{(e)}(\mathbf{x}) \} r_{\mathbf{x}} d\mathbf{s}_{\mathbf{x}} = 0 \end{aligned} \quad (16)$$

Similarly for equation (13), we have

$$\begin{aligned} & \int_{\gamma} \phi_i(\mathbf{x}) \{ [1 - c(\mathbf{x})] u^{(2)}(\mathbf{x}) \\ & \quad + \int_{\gamma} [u^{(2)}(\mathbf{y}) \partial_{\mathbf{n}_y} \mathcal{G}_k(\mathbf{x}, \mathbf{y}) - \mathcal{G}_k(\mathbf{x}, \mathbf{y}) q^{(2)}(\mathbf{y})] r_{\mathbf{y}} d\mathbf{s}_{\mathbf{y}} \} r_{\mathbf{x}} d\mathbf{s}_{\mathbf{x}} = 0 \end{aligned} \quad (17)$$

In the Galerkin BEM framework, the free-term coefficient $c(\mathbf{x})$ is set uniformly to 1/2 along γ , since variations at corner points (e.g., 1/4 for right angles) lie on a set of measure zero and thus do not affect the Lebesgue integral [10]. This convention simplifies the implementation without compromising accuracy. For the discretization, the unknown boundary fields are approximated as linear combinations of boundary basis functions:

$$\begin{aligned} u_h^{(l)}(\mathbf{y}) &= \sum_{j=1}^{N_0} u_j^{(l)} \phi_j(\mathbf{y}) \\ q_h^{(l)}(\mathbf{y}) &= \sum_{j=1}^{N_0} q_j^{(l)} \phi_j(\mathbf{y}), \quad l = 1, 2 \end{aligned} \quad (18)$$

Substituting these expansions into the Galerkin BIE (16) directly leads to a system of algebraic equations involving the discrete boundary operators:

$$(\mathbf{M} - \mathbf{K}) \mathbf{u}^{(1)} + \mathbf{V} \mathbf{q}^{(1)} = \mathbf{f} \quad (19)$$

where

$$M_{ij} = \frac{1}{2} \int_{\gamma} \phi_i(\mathbf{x}) \phi_j(\mathbf{x}) r_{\mathbf{x}} ds_{\mathbf{x}} \quad (20a)$$

$$V_{ij} = \int_{\gamma} \int_{\gamma} \phi_i(\mathbf{x}) \mathcal{G}(\mathbf{x}, \mathbf{y}) \phi_j(\mathbf{y}) r_{\mathbf{y}} ds_{\mathbf{y}} r_{\mathbf{x}} ds_{\mathbf{x}} \quad (20b)$$

$$K_{ij} = \int_{\gamma} \int_{\gamma} \phi_i(\mathbf{x}) \partial_{n_y} \mathcal{G}(\mathbf{x}, \mathbf{y}) \phi_j(\mathbf{y}) r_{\mathbf{y}} ds_{\mathbf{y}} r_{\mathbf{x}} ds_{\mathbf{x}} \quad (20c)$$

$$f_i = \int_{\gamma} \phi_i(\mathbf{x}) u^{(e)}(\mathbf{x}) r_{\mathbf{x}} ds_{\mathbf{x}} \quad (20d)$$

Similarly, the discretization of equation (17) gives

$$(\mathbf{M} + \mathbf{K}_k) \mathbf{u}^{(2)} - \mathbf{V}_k \mathbf{q}^{(2)} = \mathbf{0} \quad (21)$$

where \mathbf{V}_k and \mathbf{K}_k are obtained by replacing \mathcal{G} with \mathcal{G}_k in equations (20b) and (20c). Additionally, the following interface conditions hold on γ :

$$u^{(1)} = u^{(2)} \quad (22a)$$

$$q^{(2)} = \mu_r q^{(1)} + (\mu_r - 1) n_r \frac{u^{(1)}}{r} \quad (22b)$$

where $\mu_r = \mu/\mu_0$ is the relative permeability of the region (2). Consequently, we deduce from equations (19), (21), (22a) and (22b) that

$$\begin{bmatrix} \mathbf{M} - \mathbf{K} & \mathbf{V} \\ \mathbf{M} + \mathbf{K}_k - (\mu_r - 1) \mathbf{V}_s & -\mu_r \mathbf{V}_k \end{bmatrix} \begin{bmatrix} \mathbf{u}^{(1)} \\ \mathbf{q}^{(1)} \end{bmatrix} = \begin{bmatrix} \mathbf{f} \\ \mathbf{0} \end{bmatrix} \quad (23)$$

where

$$V_{s,ij} = \int_{\gamma} \int_{\gamma} \phi_i(\mathbf{x}) n_r(\mathbf{y}) \mathcal{G}_k(\mathbf{x}, \mathbf{y}) \phi_j(\mathbf{y}) ds_{\mathbf{y}} r_{\mathbf{x}} ds_{\mathbf{x}} \quad (24)$$

Subsequently, the impedance change of the induction coil due to the presence of the metal object can be obtained by Auld's formula [11]:

$$\Delta Z = -\frac{2\pi i\omega}{\mu_0 I^2} \int_{\gamma} (u^{(e)} q^{(1)} - u^{(1)} q^{(e)}) r ds, \quad (25)$$

where $u^{(e)}$ and $q^{(e)}$ denote the excitation vector potential and its normal derivative, respectively, and $u^{(1)}, q^{(1)}$ represent the solution fields in the non-conductive region. To discretize the impedance expression in (25), each

boundary element e is mapped from the reference interval $t \in [0, 1]$ by the isoparametric parametrization

$$\mathbf{x}_e(t) = \sum_a N_a(t) \mathbf{x}_a, \quad ds = J_e(t) dt,$$

where $N_a(t)$ denote the shape functions, $J_e(t)$ is the mapping Jacobian, and the fields $u^{(1)}, q^{(1)}$ are interpolated with the same shape functions. Let t_m, w_m be the GL points and weights on $[0, 1]$. Evaluating the excitation fields $u^{(e)}, q^{(e)}$ at $\mathbf{x}_e(t_m)$, the impedance variation is approximated by the GL quadrature

$$\Delta Z \approx -\frac{2\pi i\omega}{\mu_0 I^2} \sum_{e=1}^{N_e} \sum_{m=1}^{n_q} \left[u^{(e)}(\mathbf{x}_e(t_m)) q_e^{(1)}(t_m) - u_e^{(1)}(t_m) q^{(e)}(\mathbf{x}_e(t_m)) \right] \cdot r_e(t_m) J_e(t_m) w_m. \quad (26)$$

3. Coordinate Transformation for 2D Singular Integrals

In the Galerkin BEM framework, evaluating element integrals of the form

$$I = \int_0^1 \int_0^1 K(x(\xi), y(\eta)) \phi(\xi) \psi(\eta) J_x(\xi) J_y(\eta) d\xi d\eta \quad (27)$$

requires special treatment when the kernel K is singular. 2D boundary kernels typically exhibit either logarithmic singularities of the form $\ln|x - y|$ or Cauchy singularities $(x - y)^{-1}$ as source and field points approach coincidence [12], rendering direct tensor-product GL quadrature unreliable.

A natural starting point is the Sauter–Schwab quadrature (SSQ) [13, 14], which provides a systematic framework for regularizing singular boundary integrals through coordinate transformations. Originally developed for four-dimensional surface–surface integrals in three-dimensional BEM, the SSQ classifies element pairs into three configurations: identical panels, common edge, and common vertex. Each configuration is addressed by a tailored sequence of Duffy mappings [15].

Although the present problem is intrinsically two-dimensional, involving curve–curve interactions, the core principle of the SSQ extends naturally: singular behavior is isolated by subdividing the parameter domain and applying suitable coordinate transformations. In two dimensions, only two singular configurations arise: *Coincident elements*, whose parameter domains

overlap; and *Touching elements*, which share a common endpoint. Both cases reduce to triangular subdomains of $[0, 1]^2$, whereupon Duffy mappings regularize the integrals and yield smooth integrands amenable to GL quadrature. The coordinate transformations employed in this work are summarized below.

1. **Coincident elements:** The parameter square $[0, 1]^2$ is divided along the diagonal into two triangles. This partitioning isolates the singular line $\eta = \xi$, after which a Duffy mapping removes the singularity. For the upper triangle ($\eta > \xi$), we set

$$\xi = u, \quad \eta = u + (1 - u)v, \quad (u, v) \in [0, 1]^2, \quad (28)$$

and for the lower triangle ($\xi > \eta$),

$$\eta = u, \quad \xi = u + (1 - u)v. \quad (29)$$

In both cases the Jacobian contributes a factor $|\det J| = (1 - u)$, which transfers the singular behavior from the diagonal $\eta = \xi$ to the coordinate edge $v = 0$ and simultaneously weakens it. The upper triangle contributes

$$\begin{aligned} I_1 = \int_0^1 \int_0^1 & K(x(u), y(u + (1 - u)v)) \phi(u) \psi(u + (1 - u)v) \\ & \cdot J_x(u) J_y(u + (1 - u)v) (1 - u) \, du \, dv, \end{aligned} \quad (30)$$

while the lower triangle yields an analogous expression I_2 with the roles of ξ and η interchanged. The full coincident integral is therefore

$$I = I_1 + I_2. \quad (31)$$

It is well established that the Duffy mapping regularizes the weakly singular kernel $\ln|x - y|$ [16]. We emphasize further that kernels with Cauchy singularities $(x - y)^{-1}$ are likewise regularized by this transformation, yielding integrals that can be evaluated accurately via standard GL quadrature on the unit square (see Appendix A). Additionally, a graded substitution $v = w^p$ with $p > 1$ can be introduced to cluster quadrature points near $v = 0$, further enhancing the convergence rate.

2. **Touching elements:** When two elements share a common endpoint, the kernel singularity occurs at a corner of the parameter square $[0, 1]^2$ —for

instance, at $(\xi, \eta) = (1, 0)$. To handle this case, we partition the square into two triangles and map each triangle to the unit square via a Duffy transformation.

For the triangle containing the singular corner, the mapping is

$$\xi = 1 - u, \quad \eta = uv, \quad (u, v) \in [0, 1]^2, \quad (32)$$

with Jacobian $d\xi d\eta = u du dv$. A local expansion near the touching point $x(1) = y(0)$ shows that

$$|x(\xi) - y(\eta)| \approx u |x'(1) + v y'(0)|,$$

so the weakly singular kernel behaves as $K \sim \ln u$, and the Jacobian factor u cancels this logarithmic singularity.

For Cauchy-singular kernels, near $(\xi, \eta) = (1, 0)$ the integrand admits the representation

$$K(x(\xi), y(\eta)) \phi(\xi) \psi(\eta) J_x(\xi) J_y(\eta) = \frac{A(\xi, \eta)}{(1 - \xi) + \eta}, \quad (33)$$

where $A(\xi, \eta)$ is bounded and smooth over $[0, 1]^2$. Applying the mapping (32) yields

$$\begin{aligned} I_{\text{sing}} &= \int_0^1 \int_0^1 \frac{A(1 - u, uv)}{u(1 + v)} u du dv \\ &= \int_0^1 \int_0^1 \frac{A(1 - u, uv)}{1 + v} du dv, \end{aligned} \quad (34)$$

which is fully regular over $[0, 1]^2$. The complete transformed integral for the singular triangle is thus

$$\begin{aligned} I_{\text{sing}} &= \int_0^1 \int_0^1 K(x(1 - u), y(uv)) \phi(1 - u) \psi(uv) \\ &\quad \cdot J_x(1 - u) J_y(uv) u du dv. \end{aligned} \quad (35)$$

For the complementary triangle, we employ the mapping

$$\xi = u, \quad \eta = 1 - u + uv, \quad (u, v) \in [0, 1]^2, \quad (36)$$

with Jacobian $d\xi d\eta = u du dv$. In this region no $1/u$ singularity arises; indeed, near the corner $(u, v) = (1, 0)$ we have

$$(1 - \xi) + \eta = (1 - u) + (1 - u + uv) = 2(1 - u) + uv > 0$$

throughout $[0, 1]^2$. The corresponding regular contribution is

$$I_{\text{reg}} = \int_0^1 \int_0^1 K(x(u), y(1 - u + uv)) \phi(u) \psi(1 - u + uv) \cdot J_x(u) J_y(1 - u + uv) u du dv, \quad (37)$$

which is smooth and amenable to direct GL quadrature.

The full touching integral is then

$$I = I_{\text{sing}} + I_{\text{reg}}.$$

This decomposition eliminates the endpoint singularity at $(1, 0)$, yielding two regular double integrals over the unit square that apply uniformly to basis functions of any polynomial order.

In practical BEM implementations, singular Helmholtz kernels are often treated by analytically extracting the singular part and evaluating it in closed form [7]. This approach, however, yields element-order-dependent expressions whose complexity grows rapidly with polynomial degree. In the present work, we still isolate the singular component of the Helmholtz kernels, but its evaluation is handled entirely through the proposed coordinate transformations, while the smooth remainder is integrated using standard GL rules. Consequently, no order-specific analytic formulas are required, and the same quadrature framework applies uniformly across all element orders. This unified treatment substantially simplifies higher-order Galerkin boundary element implementations.

4. Numerical Validation of Axisymmetric Galerkin BEM

To evaluate the accuracy and convergence characteristics of the proposed formulation, three representative axisymmetric configurations are analyzed: a cylindrical tube, a conical tube, and a spherical shell. In each case, the impedance change of an axisymmetric eddy-current coil positioned in proximity to a conducting structure is computed. A common coil geometry is

employed across all simulations (Table 1). The coil’s source potential $A_\varphi^{(e)}$ and its normal derivative are obtained through analytical expressions provided in Appendix B. Impedance variations are normalized and reported as $\Delta R/X_0$ and $\Delta X/X_0$, where $X_0 = \omega L_0$ denotes the reactance of the isolated coil with self-inductance L_0 (Table 1).

Table 1: Common coil parameters used in all validation cases.

Parameter	Symbol	Value
Inner radius (m)	r_1	0.007
Outer radius (m)	r_2	0.0085
Half-height (m)	h	0.002
Turns	N	500
Baseline inductance (mH)	L_0	4.740 562 2

4.1. A coil placed inside a S30400 stainless steel tube

We consider a coaxial eddy-current inspection configuration in which a cylindrical coil is placed inside a stainless-steel tube (AISI 304, UNS S30400). The tube has inner and outer radii a_1 , a_2 , and axial length l , while the coil has inner and outer radii r_1 and r_2 and half-height h . The unit normal on the tube boundary is taken as outward-pointing.

The conductive tube (region 2) is characterized by relative permeability μ_r and conductivity σ , giving rise to the complex wavenumber $k = \sqrt{-i\omega\mu_0\mu_r\sigma}$. The tube surface is discretized with linear boundary elements, and all singular integrals are evaluated using the algorithm in §3. Two axial coil positions, distinguished by the offset parameter z_0 , are examined. For each position, the coil impedance is computed over a range of frequencies. Figure 2 presents the normalized impedance variations $\Delta R/X_0$ and $\Delta X/X_0$ as functions of frequency; BEM predictions appear as solid and dashed curves, while reference FEM solutions are indicated by discrete markers (circles and triangles). Excellent agreement is observed between the two methods.

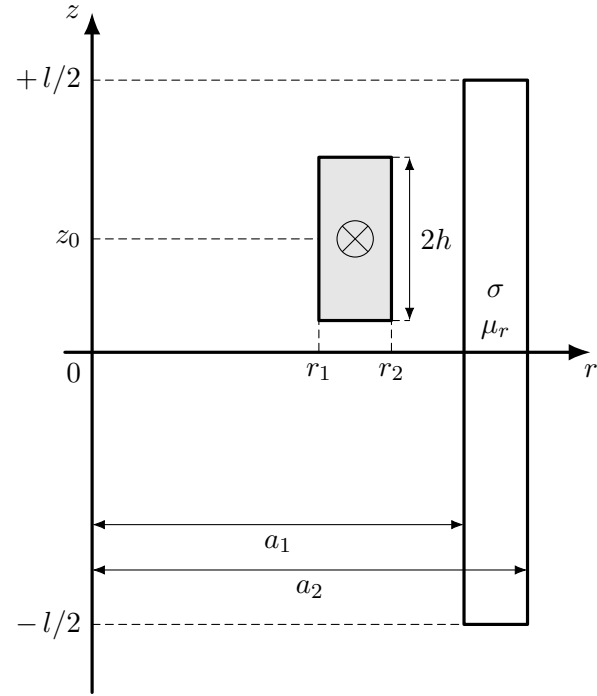


Figure 1: Side view of a stainless-steel tube and a coaxial coil with center at z_0 .

Table 2: Geometric and material parameters for the S30400 stainless-steel tube.

Parameter	Symbol	Value
Inner tube radius (m)	a_1	0.009
Outer tube radius (m)	a_2	0.011
Tube length (m)	l	0.024
Relative permeability	μ_r	1.021
Conductivity (MS/m)	σ	1.37

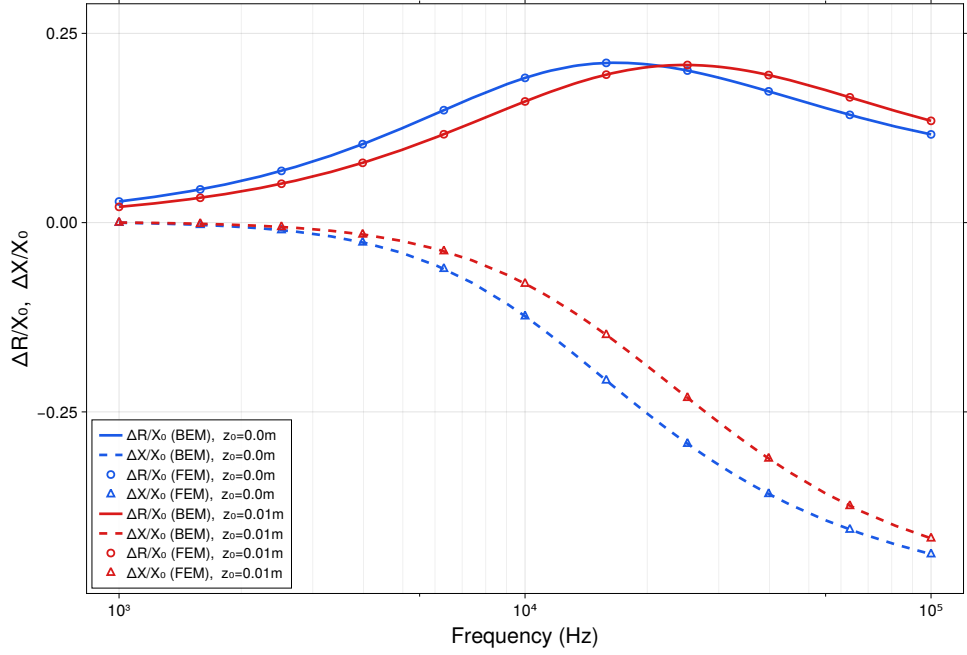


Figure 2: Comparison of $\Delta R/X_0$ and $\Delta X/X_0$ obtained by the Galerkin BEM and FEM benchmark for the S30400 tube at two lift-off positions.

4.2. A coil located inside a 7075-T6 aluminum conical tube

We next consider a conical tube fabricated from 7075-T6 aluminum, with inner and outer radii that vary linearly along the z -axis. The smaller end of the tube is located at $z = -l/2$ and the larger end at $z = +l/2$, maintaining a uniform wall thickness throughout. The geometry is illustrated in Fig. 3. The coil parameters remain identical to those of the preceding cylindrical case.

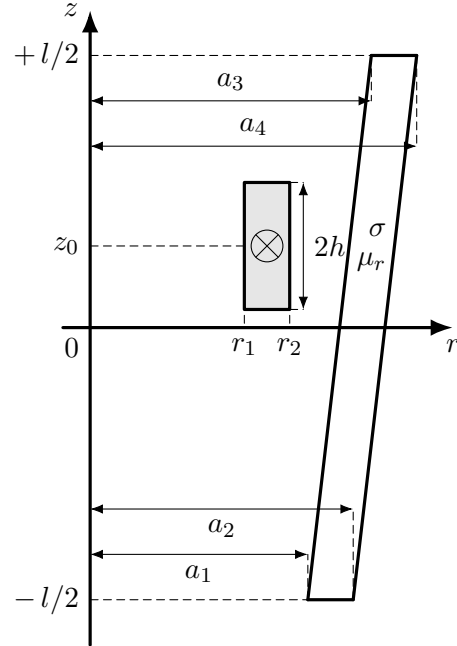


Figure 3: Side view of a conical conductive tube with bottom radii (a_1, a_2) at $z = -l/2$ and top radii (a_3, a_4) at $z = +l/2$, and a coaxial coil centered at z_0 .

For the conical tube validation, the slanted boundary profile is discretized with linear elements, and all singular integrals are evaluated using the algorithm in §3. Impedance variations are computed for three axial coil positions z_0 over the same frequency range as in the cylindrical case. The normalized resistance and reactance changes $\Delta R/X_0$ and $\Delta X/X_0$, obtained via Auld's formula, are compared with FEM reference data in Figure 4. BEM predictions appear as solid and dashed curves, while FEM solutions are denoted by circles and triangles. Excellent agreement is achieved across all frequencies and coil positions.

Table 3: Geometric and material parameters for the conical 7075–T6 aluminum tube.

Parameter	Symbol	Value
Bottom inner radius (m)	a_1	0.0090
Bottom outer radius (m)	a_2	0.0106
Top inner radius (m)	a_3	0.0108
Top outer radius (m)	a_4	0.0124
Tube length (m)	l	0.022
Relative permeability	μ_r	1.0
Conductivity (MS/m)	σ	16.93

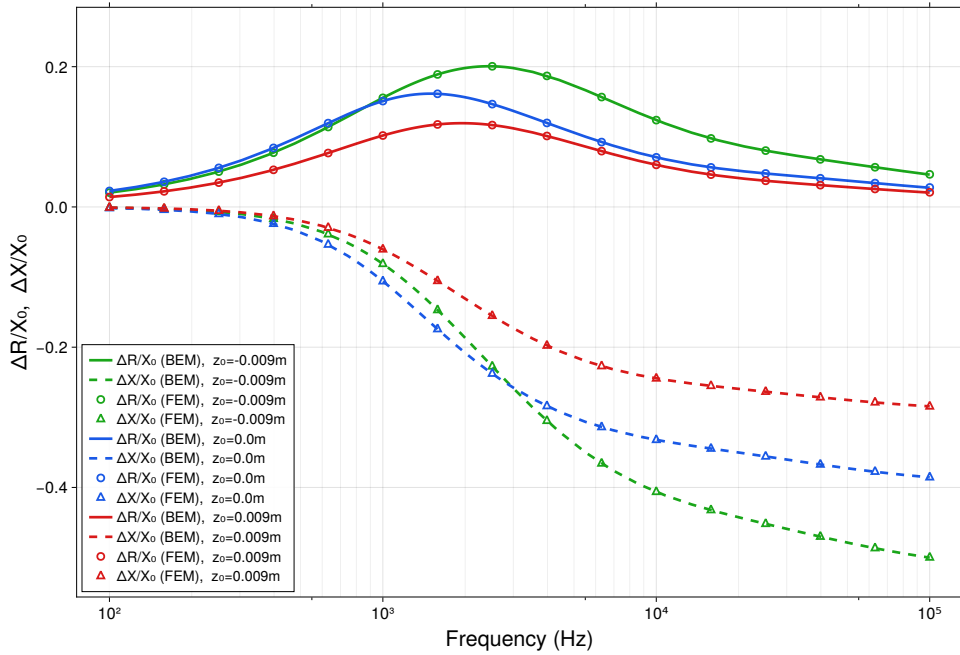


Figure 4: Comparison of $\Delta R/X_0$ and $\Delta X/X_0$ obtained by the Galerkin BEM and the FEM benchmark for the conical 7075–T6 tube at different axial positions of the coil.

4.3. A coil placed near a C96400 copper alloy spherical shell

The third validation examines a spherical shell fabricated from C96400 copper alloy [17], with the coil positioned either external or internal to the

shell. This geometry provides a more stringent test of the numerical framework, as the curved boundary demands accurate integration over non-planar segments and introduces global coupling among disjoint regions. Coil specifications are given in Table 1, while shell dimensions and material properties appear in Table 4. The configuration is illustrated schematically in Figure 5.

All singular kernels are evaluated using the algorithm detailed in §3, ensuring numerical accuracy for every element interaction. Impedance variations are computed at two axial coil positions, and the normalized components $\Delta R/X_0$ and $\Delta X/X_0$, obtained via Auld's formula, are compared with high-fidelity FEM. Figure 6 presents the frequency-dependent response; close agreement between boundary-element predictions and reference solutions is observed throughout the parameter range investigated. This consistency confirms the method's ability to treat curved geometries with high accuracy.

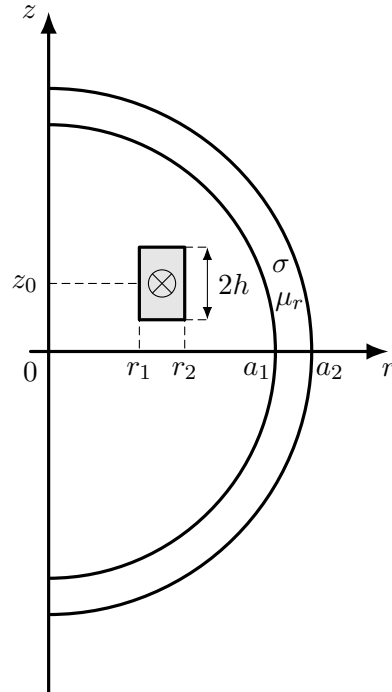


Figure 5: Side view of a spherical shell and a coil centered at z_0 .

Table 4: Geometric and material parameters for the C96400 spherical shell.

Parameter	Symbol	Value
Inner radius (m)	a_1	0.011
Outer radius (m)	a_2	0.012
Relative permeability	μ_r	1.0
Conductivity (MS/m)	σ	2.9

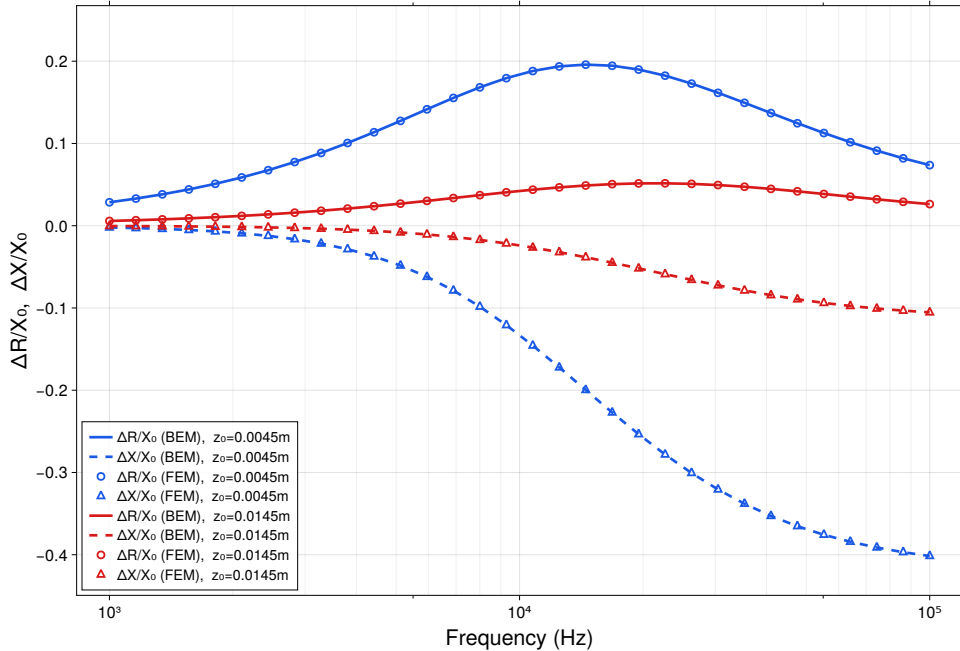


Figure 6: Comparison of $\Delta R/X_0$ and $\Delta X/X_0$ obtained by the Galerkin BEM and the FEM benchmark for the C96400 spherical shell at two axial positions of the coil.

Table 5 summarizes the relative errors and average CPU time per frequency point for both the P_1 (linear) and P_2 (quadratic isoparametric) Galerkin BEM formulations applied to the spherical shell. The mesh parameter n_s specifies the boundary discretization. Relative errors for the P_1 formulation

are defined as

$$\begin{aligned}\epsilon_R^{P_1} &= \frac{\|(\Delta R/X_0)_{P_1} - (\Delta R/X_0)_{\text{ref}}\|_2}{\|(\Delta R/X_0)_{\text{ref}}\|_2} \times 100\%, \\ \epsilon_X^{P_1} &= \frac{\|(\Delta X/X_0)_{P_1} - (\Delta X/X_0)_{\text{ref}}\|_2}{\|(\Delta X/X_0)_{\text{ref}}\|_2} \times 100\%,\end{aligned}\quad (38)$$

where $(\Delta R/X_0)_{\text{ref}}$ and $(\Delta X/X_0)_{\text{ref}}$ denote FEM reference values. The quantities $\epsilon_R^{P_2}$ and $\epsilon_X^{P_2}$ are defined analogously for the P_2 formulation. The entries t_{P_1} and t_{P_2} report the average CPU time in seconds required to solve a single frequency point after pre-compilation. All computations were performed in Julia on a laptop equipped with an AMD Ryzen AI 9 HX 370 processor (2.0 GHz) and 32 GB of RAM. For the FEM reference solution, we set the maximum element size of $50\ \mu\text{m}$ within the conducting shell. This ensured that the mesh resolves the smallest skin depth with approximately 20 layers of elements, making the FEM error negligible.

Convergence analysis reveals distinct behavior for the two element types. The P_1 formulation exhibits classical second-order convergence: relative errors in both ΔR and ΔX decrease monotonically with increasing n_s , consistent with the expected $O(h^2)$ asymptotic rate. In contrast, the P_2 formulation achieves relative errors on the order of 10^{-5} even on the coarsest mesh, with negligible improvement upon further refinement. This saturation arises from the superior approximation properties of quadratic isoparametric elements: when applied to the smooth field distributions characteristic of the spherical geometry, discretization errors are reduced to levels comparable to numerical integration tolerances and finite-precision arithmetic limits. Consequently, P_2 impedance predictions remain effectively invariant across the mesh densities tested, whereas P_1 results converge systematically toward the reference solution at the theoretically predicted rate.

Table 5: Relative errors with respect to FEM and average CPU time per frequency point (Spherical Shell, $z_0 = 0.0045\ \text{m}$).

n_s	$\epsilon_R^{P_1}\ [\%]$	$\epsilon_X^{P_1}\ [\%]$	$t_{P_1}\ [\text{s}]$	$\epsilon_R^{P_2}\ [\%]$	$\epsilon_X^{P_2}\ [\%]$	$t_{P_2}\ [\text{s}]$
40	0.228	0.183	0.39	0.00665	0.00761	1.04
80	0.0613	0.0492	1.40	0.00587	0.00693	3.81
160	0.0192	0.0164	7.06	0.00549	0.00635	15.46
320	0.00843	0.00797	26.21	0.00506	0.00571	70.53

5. Conclusion

A general, high-accuracy Galerkin BEM for axisymmetric eddy-current analysis has been developed. The principal technical contribution is a set of Duffy coordinate transformations that regularize both logarithmic and Cauchy singularities arising from coincident and touching element configurations. These mappings convert all singular integrals into smooth integrands over the unit square, eliminating the need for analytic singularity extraction and enabling straightforward GL quadrature for elements of arbitrary order.

Benchmark problems involving cylindrical, conical, and spherical conductors validate the method's accuracy and robustness. Linear elements exhibit classical second-order convergence, while quadratic elements achieve relative errors on the order of 10^{-5} even on coarse meshes. The formulation is compact, broadly applicable, and readily extensible to fast multipole or \mathcal{H} -matrix acceleration, as well as to other 2D Galerkin BEM beyond eddy-current testing.

Appendix A. Regularization of Cauchy-singular kernels of coincident elements under the symmetric split Duffy mapping

For coincident boundary elements that share the same smooth parametrization, the Cauchy-singular kernel in equation (27) of §3 can be written in the standard form

$$K(x(\xi), y(\eta))\phi(\xi)\psi(\eta)J_x(\xi)J_y(\eta) = \frac{F(\xi, \eta)}{\xi - \eta}, \quad (\text{A1})$$

where $F(\xi, \eta)$ is a smooth function on $[0, 1]^2$. Then, the equation (27) can be written in the principal-value sense as

$$I = \text{p. v.} \int_0^1 \int_0^1 \frac{F(\xi, \eta)}{\xi - \eta} d\xi d\eta. \quad (\text{A2})$$

Here ϕ, ψ are the shape functions of arbitrary order associated with the test and trial factors.

To isolate the singular line $\eta = \xi$, we split the unit square into the upper and lower triangles

$$T_1 = \{(\xi, \eta) \in [0, 1]^2 : \eta > \xi\}, \quad T_2 = \{(\xi, \eta) \in [0, 1]^2 : \xi > \eta\},$$

so that

$$I = \int_{T_1} \frac{F(\xi, \eta)}{\xi - \eta} d\xi d\eta + \int_{T_2} \frac{F(\xi, \eta)}{\xi - \eta} d\xi d\eta = I_1 + I_2. \quad (\text{A3})$$

For T_1 we use the Duffy mapping

$$\xi = u, \quad \eta = u + (1 - u)v, \quad (u, v) \in [0, 1]^2, \quad (\text{A4})$$

which maps the unit square in (u, v) onto the upper triangle $\eta > \xi$. The Jacobian determinant is

$$\left| \frac{\partial(\xi, \eta)}{\partial(u, v)} \right| = 1 - u.$$

Moreover,

$$\xi - \eta = -(1 - u)v.$$

Thus

$$\begin{aligned} I_1 &= \int_0^1 \int_0^1 \frac{F(u, u + (1 - u)v)}{-(1 - u)v} (1 - u) du dv \\ &= - \int_0^1 \int_0^1 \frac{F(u, u + (1 - u)v)}{v} du dv. \end{aligned} \quad (\text{A5})$$

For T_2 we use the symmetric mapping

$$\xi = u + (1 - u)v, \quad \eta = u, \quad (u, v) \in [0, 1]^2, \quad (\text{A6})$$

with the same Jacobian $|J| = 1 - u$ and

$$\xi - \eta = (1 - u)v.$$

Hence

$$\begin{aligned} I_2 &= \int_0^1 \int_0^1 \frac{F(u + (1 - u)v, u)}{(1 - u)v} (1 - u) du dv \\ &= \int_0^1 \int_0^1 \frac{F(u + (1 - u)v, u)}{v} du dv. \end{aligned} \quad (\text{A7})$$

Adding (A5) and (A7) yields the transformed representation

$$I = \int_0^1 \int_0^1 \frac{F(u + (1 - u)v, u) - F(u, u + (1 - u)v)}{v} du dv. \quad (\text{A8})$$

The apparent singular factor $1/v$ is now multiplied by a difference of two evaluations of the same smooth function F . We now show that this difference

cancels the Cauchy singularity and yields a bounded integrand on the whole $[0, 1]^2$.

For any fixed $u \in [0, 1]$, since $F(\xi, \eta) \in C^1([0, 1]^2)$, a Taylor expansion of $F(\xi, \eta)$ about the point (u, u) gives, for small v ,

$$F(u + (1 - u)v, u) = F(u, u) + (1 - u)v F'_\xi(u, u) + O(v^2), \quad (\text{A9})$$

$$F(u, u + (1 - u)v) = F(u, u) + (1 - u)v F'_\eta(u, u) + O(v^2), \quad (\text{A10})$$

Subtracting these two expansions, we obtain

$$\begin{aligned} & F(u + (1 - u)v, u) - F(u, u + (1 - u)v) \\ &= (1 - u)v [F'_\xi(u, u) - F'_\eta(u, u)] + O(v^2). \end{aligned} \quad (\text{A11})$$

Hence, as $v \rightarrow 0$, we obtain a regular integrand on the closed square $[0, 1]^2$

$$\begin{aligned} & \lim_{v \rightarrow 0} \frac{F(u + (1 - u)v, u) - F(u, u + (1 - u)v)}{v} \\ &= (1 - u) [F'_\xi(u, u) - F'_\eta(u, u)]. \end{aligned} \quad (\text{A12})$$

We have thus shown that the Duffy mapping of the two triangles, followed by their recombination in (A8), transforms the original Cauchy-singular kernel into a regular integrand. The line singularity $\eta = \xi$ is converted into a simple algebraic factor that is exactly cancelled by the antisymmetric difference of the two evaluations of F . As a consequence, the coincident-element integral I can be evaluated by standard tensor-product GL quadrature on the unit square, with the same convergence properties as for a smooth 2D integrand. In particular, no explicit analytical singularity extraction is required, and the argument applies uniformly to any element order.

A subtle issue arises regarding the *discrete* stability of the tensor-product GL quadrature applied to the transformed representation (A8). Although the integrand in (A8) is regular, one must verify that no numerical instability arises from the clustering of GL nodes near $v = 0$ under the Duffy mapping. In particular, each quadrature term contains an effective factor w_j/v_j , and it is not *a priori* evident that this ratio remains bounded as $v_j \rightarrow 0$.

We now demonstrate that the GL rule is fully stable. Let $\{x_j, w_j\}_{j=1}^n$ denote the GL nodes and weights on $[-1, 1]$. Near the endpoint $x = 1$, the Mehler–Heine formula [18] supplies the well-known Bessel correspondence

$$\lim_{n \rightarrow \infty} P_n \left(\cos \frac{z}{n} \right) = \lim_{n \rightarrow \infty} P_n \left(1 - \frac{z^2}{2n^2} \right) = J_0(z), \quad (\text{A13})$$

from which it follows that the nodes near $x = 1$ satisfy

$$x_j = 1 - \frac{j_{0,j}^2}{2n^2} + O(n^{-4}), \quad v_j = \frac{1 - x_j}{2} = \frac{j_{0,j}^2}{4n^2} + O(n^{-4}), \quad (\text{A14})$$

where $j_{0,j}$ is the j -th positive zero of the Bessel function J_0 . Although the Mehler–Heine formula is an asymptotic statement as $n \rightarrow \infty$, the corresponding approximation of the GL nodes near $x = 1$ is already good for moderately small orders (e.g., $n \approx 10$). For the GL weights we use the exact identity

$$w_j = \frac{2}{(1 - x_j^2) [P'_n(x_j)]^2},$$

together with the endpoint derivative asymptotic

$$P'_n(x_j) = -\frac{n^2}{j_{0,j}} J_1(j_{0,j}) + O(n), \quad (\text{A15})$$

again derived from the Mehler–Heine expansion and its derivative. Substituting these relations yields

$$w_j = \frac{2}{n^2 J_1^2(j_{0,j})} + O(n^{-4}). \quad (\text{A16})$$

Combining (A14) and (A16), the effective factor in (A8) becomes

$$\frac{w_j}{v_j} = \frac{8}{j_{0,j}^2 J_1^2(j_{0,j})} + O(n^{-2}), \quad (\text{A17})$$

a finite positive constant depending only on the Bessel zeros. Thus no term grows with n , and no near-cancellation of large quantities can arise near $v = 0$. We conclude that the tensor–product GL quadrature is *asymptotically stable* under the endpoint clustering, fully consistent with the analytical regularity established in (A8).

To complement the analytical regularity and stability proofs, we present a numerical experiment demonstrating that the symmetric Duffy mapping, combined with tensor–product GL rules, yields machine–precision accuracy for Cauchy integrals. Consider the principal–value integral

$$I = \text{p. v.} \int_0^1 \int_0^1 \frac{\phi(\xi) \psi(\eta)}{\eta - \xi} d\xi d\eta, \quad \phi(\xi) = \xi^3, \quad \psi(\eta) = 1 - \eta^3, \quad (\text{A18})$$

whose exact value is

$$I_{\text{exact}} = -\frac{11}{24}.$$

The integral is evaluated using the coincident–element Duffy transformation and standard GL rules in (u, v) coordinates. Table A1 summarizes the results. For $n_q \geq 6$, the error reaches the level of 10^{-15} to 10^{-16} .

Table A1: Numerical evaluation of the Cauchy integral A(18) using tensor–product GL quadrature after the symmetric Duffy mapping.

n_q	I_{num}	Error $ I_{\text{num}} - I_{\text{exact}} $
4	-0.458 316 326 530 611 99	1.7×10^{-5}
6	-0.458 333 333 333 333 31	$< 1.0 \times 10^{-16}$
8	-0.458 333 333 333 334 04	7.2×10^{-16}
10	-0.458 333 333 333 332 98	3.3×10^{-16}
12	-0.458 333 333 333 332 87	4.4×10^{-16}
16	-0.458 333 333 333 332 93	3.9×10^{-16}
20	-0.458 333 333 333 333 26	$< 1.0 \times 10^{-16}$
24	-0.458 333 333 333 333 15	1.7×10^{-16}
32	-0.458 333 333 333 332 93	3.9×10^{-16}

Together with the Mehler–Heine analysis, this example provides strong numerical evidence that the proposed transformation yields a uniformly stable and high–accuracy discretization of Cauchy-singular integrals for Galerkin BEM.

Appendix B. Expressions of source field of cylindrical coil

Consider a cylindrical coil centered at $(0, 0, z_0)$ in cylindrical coordinates (r, ϕ, z) , with inner and outer radii r_1, r_2 , axial length $2h$, and N turns. The coil carries an alternating current with amplitude I and angular frequency ω . The electromagnetic field generated by such a coil can be expressed in terms of elliptic integrals [19]. Due to the axial symmetry of the configuration, only

the φ -component of the vector potential is non-zero

$$A_\varphi^{(e)}(r, \zeta) = \frac{\mu_0 NI}{4h(r_2 - r_1)} \times \begin{cases} \int_{r_1}^{r_2} \rho [f_1(\rho, r, -h - \zeta) - f_1(\rho, r, h - \zeta)] d\rho & \zeta \leq -h \\ \int_{r_1}^{r_2} \rho [f_1(\rho, r, \zeta - h) - f_1(\rho, r, \zeta + h)] d\rho & \zeta \geq h \\ g_1(r) - \int_{r_1}^{r_2} \rho [f_1(\rho, r, \zeta + h) + f_1(\rho, r, h - \zeta)] d\rho & -h < \zeta < h \end{cases} \quad (\text{B1})$$

where $\zeta = z - z_0$, and

$$\begin{aligned} f_1(\rho, r, \zeta) &= \int_0^\infty J_1(\lambda r) J_1(\lambda \rho) \frac{e^{-\zeta \lambda}}{\lambda} d\lambda \\ &= \frac{\zeta}{\pi \sqrt{\rho r}} \left[\frac{\mathbf{E}(\alpha)}{\sqrt{\alpha}} - \frac{(2\rho^2 + 2r^2 + \zeta^2)\sqrt{\alpha} \mathbf{K}(\alpha)}{4\rho r} \right] \\ &\quad + \frac{1}{2} \begin{cases} \frac{\rho^2 - r^2}{2\rho r} \Lambda_0(\beta, \alpha) + \frac{r}{\rho} & r < \rho \\ \frac{r^2 - \rho^2}{2\rho r} \Lambda_0(\beta, \alpha) + \frac{\rho}{r} & r > \rho \end{cases} \end{aligned} \quad (\text{B2})$$

and

$$g_1(r) = \begin{cases} (r_2 - r_1)r & r \leq r_1 \\ -\frac{2}{3}r^2 + r_2 r - \frac{r_1^3}{3r} & r_1 < r < r_2 \\ \frac{r_2^3 - r_1^3}{3r} & r \geq r_2 \end{cases} \quad (\text{B3})$$

with

$$\alpha = \frac{4\rho r}{(\rho + r)^2 + \zeta^2}$$

and

$$\beta = \arcsin \frac{\zeta}{\sqrt{(r - \rho)^2 + \zeta^2}}$$

In equation (B2), $\mathbf{K}(\alpha)$, $\mathbf{E}(\alpha)$ are the complete elliptic integrals of the first and second kind, Λ_0 is the Heuman Lambda function

$$\Lambda_0(\beta, \alpha) = \frac{2}{\pi} [\mathbf{E}(\alpha)F(\beta, \alpha') + \mathbf{K}(\alpha)E(\beta, \alpha') - \mathbf{K}(\alpha)F(\beta, \alpha')]$$

where $\alpha' = 1 - \alpha$, $F(\beta, \alpha')$ and $E(\beta, \alpha')$ are the incomplete elliptic integrals of the first and second kinds, respectively. The magnetic source field $B_z^{(e)}$ is

$$B_z^{(e)}(r, \zeta) = \frac{\mu_0 NI}{4h(r_2 - r_1)} \times \begin{cases} \int_{r_1}^{r_2} \rho [f_2(\rho, r, -h - \zeta) - f_2(\rho, r, h - \zeta)] d\rho & \zeta \leq -h \\ \int_{r_1}^{r_2} \rho [f_2(\rho, r, \zeta - h) - f_2(\rho, r, \zeta + h)] d\rho & \zeta \geq h \\ g_2(r) - \int_{r_1}^{r_2} \rho [f_2(\rho, r, \zeta + h) + f_2(\rho, r, h - \zeta)] d\rho & -h < \zeta < h \end{cases} \quad (\text{B4})$$

where

$$\begin{aligned} f_2(\rho, r, \zeta) &= \int_0^\infty J_0(\lambda r) J_1(\lambda \rho) e^{-\zeta \lambda} d\lambda \\ &= \frac{1}{\rho} \cdot \begin{cases} 1 - \frac{\zeta \sqrt{\alpha} \mathbf{K}(\alpha)}{2\pi\sqrt{\rho r}} - \frac{\Lambda_0(\beta, \alpha)}{2} & r < \rho \\ -\frac{\zeta \sqrt{\alpha} \mathbf{K}(\alpha)}{2\pi\sqrt{\rho r}} + \frac{\Lambda_0(\beta, \alpha)}{2} & r > \rho \end{cases} \end{aligned} \quad (\text{B5})$$

and

$$g_2(r) = \begin{cases} 2(r_2 - r_1) & r \leq r_1 \\ 2(r_2 - r) & r_1 < r < r_2 \\ 0 & r \geq r_2 \end{cases} \quad (\text{B6})$$

The magnetic source field $B_r^{(e)}$ is

$$B_r^{(e)}(r, \zeta) = \frac{\mu_0 NI}{4h(r_2 - r_1)} \int_{r_1}^{r_2} \rho [f_3(\rho, r, |h - \zeta|) - f_3(\rho, r, |h + \zeta|)] d\rho \quad (\text{B7})$$

where

$$\begin{aligned} f_3(\rho, r, \zeta) &= \int_0^\infty J_1(\lambda r) J_1(\lambda \rho) e^{-\zeta \lambda} d\lambda \\ &= \frac{1}{\pi\sqrt{\alpha\rho r}} [(2 - \alpha)\mathbf{K}(\alpha) - 2\mathbf{E}(\alpha)] \end{aligned} \quad (\text{B8})$$

For the Auld's formula, the normal derivative of the vector potential is

$$\partial_n A_\varphi^{(e)} = n_r \partial_r A_\varphi^{(e)} + n_z \partial_z A_\varphi^{(e)} \quad (\text{B9})$$

where

$$\partial_r A_\varphi^{(e)} = B_z^{(e)} - A_\varphi^{(e)}/r \quad (\text{B10})$$

and

$$\partial_z A_\varphi^{(e)} = -B_r^{(e)} = -\frac{\mu_0 NI}{4h(r_2 - r_1)} \int_{r_1}^{r_2} \rho [f_3(\rho, r, |h - \zeta|) - f_3(\rho, r, |h + \zeta|)] d\rho \quad (\text{B11})$$

When $r = 0$, the above field components reduce to

$$A_\varphi^{(e)}(0, \zeta) = 0 \quad (\text{B12})$$

$$B_r^{(e)}(0, \zeta) = 0 \quad (\text{B13})$$

$$\begin{aligned} B_z^{(e)}(0, \zeta) &= \frac{\mu_0 NI}{4h(r_2 - r_1)} \\ &\times \left[(\zeta + h) \ln \frac{r_2 + \sqrt{r_2^2 + (\zeta + h)^2}}{r_1 + \sqrt{r_1^2 + (\zeta + h)^2}} - (\zeta - h) \ln \frac{r_2 + \sqrt{r_2^2 + (\zeta - h)^2}}{r_1 + \sqrt{r_1^2 + (\zeta - h)^2}} \right] \end{aligned} \quad (\text{B14})$$

and

$$\partial_r A_\varphi^{(e)}(0, \zeta) = \frac{1}{2} B_z^{(e)}(0, \zeta) \quad (\text{B15})$$

Appendix C. Axisymmetric kernel of a ring source

The axisymmetric Laplace kernel \mathcal{G} is

$$\begin{aligned} \mathcal{G}(r, z; r', z') &= \frac{1}{4\pi} \int_0^{2\pi} \frac{\cos(\varphi)}{R(\varphi)} d\varphi \\ &= \frac{1}{2} \int_0^\infty J_1(\lambda r) J_1(\lambda r') e^{-\lambda|z-z'|} d\lambda \\ &= \frac{1}{\pi\sqrt{mrr'}} \left[\left(1 - \frac{m}{2}\right) K(m) - E(m) \right] \end{aligned} \quad (\text{C1})$$

where

$$R(\varphi) = \sqrt{r^2 + r'^2 - 2rr' \cos(\varphi) + (z - z')^2}$$

and

$$m = \frac{4rr'}{(r + r')^2 + (z - z')^2}, \quad (\text{C2})$$

The components for partial derivatives are

$$\begin{aligned}\partial_{r'}\mathcal{G} &= \frac{r}{2\pi(mrr')^{3/2}} \left\{ m \left[\left(\frac{m}{2} - 1 \right) K(m) + E(m) \right] \right. \\ &\quad \left. + \frac{m_{r'}r'}{m-1} \left[(1-m)K(m) + \left(\frac{m}{2} - 1 \right) E(m) \right] \right\}\end{aligned}\quad (\text{C3})$$

and

$$\partial_{z'}\mathcal{G} = \frac{m_{z'}rr'}{2\pi(m-1)(mrr')^{3/2}} \left[(1-m)K(m) + \left(\frac{m}{2} - 1 \right) E(m) \right] \quad (\text{C4})$$

where

$$m_{r'} = \frac{4r[r^2 - r'^2 + (z - z')^2]}{[(r + r')^2 + (z - z')^2]^2} \quad (\text{C5})$$

and

$$m_{z'} = \frac{8rr'(z - z')}{[(r + r')^2 + (z - z')^2]^2} \quad (\text{C6})$$

When $r = 0$, we have $J_1(\lambda r) = 0$. Hence, from the Bessel integral expression it is easy to conclude that

$$\mathcal{G}(0, z; r', z') = 0, \quad \partial_{r'}\mathcal{G}(0, z; r', z') = 0, \quad \partial_{z'}\mathcal{G}(0, z; r', z') = 0.$$

When $r' = 0$, we have $\mathcal{G}(r, z; 0, z') = 0$, $\partial_{z'}\mathcal{G}(r, z; 0, z') = 0$, and

$$\partial_{r'}\mathcal{G}(r, z; 0, z') = \frac{r}{4\chi^3} \quad (\text{C7})$$

where

$$\chi = \sqrt{r^2 + (z - z')^2} \quad (\text{C8})$$

The axisymmetric Helmholtz kernel \mathcal{G}_k is

$$\begin{aligned}\mathcal{G}_k &= \frac{1}{4\pi} \int_0^{2\pi} \frac{e^{-ikR(\varphi)}}{R(\varphi)} \cos(\varphi) d\varphi \\ &= \frac{1}{2} \int_0^\infty J_1(\lambda r) J_1(\lambda r') \frac{\lambda}{\sqrt{\lambda^2 - k^2}} e^{-\sqrt{\lambda^2 - k^2}|z - z'|} d\lambda\end{aligned}\quad (\text{C9})$$

The Bessel integral expression (C9) is derived from [20] and the Graf's addition theorem [21]. In practice, we use singularity extraction

$$\mathcal{G}_k = \frac{1}{4\pi} \int_0^{2\pi} \frac{e^{-ikR(\varphi)} - 1}{R(\varphi)} \cos(\varphi) d\varphi + \mathcal{G} \quad (\text{C10})$$

The integral corresponding to the first term on the right-hand side of equation (C10) can be evaluated accurately using GL quadrature. The second term contains the Laplace kernel, whose singularity requires the regularization technique in § 3. An analogous approach applies to the partial derivatives of the Helmholtz kernel:

$$\begin{aligned} \partial_{r'} \mathcal{G}_k &= \frac{1}{4\pi} \int_0^{2\pi} \frac{(r' - r \cos(\varphi)) \cos(\varphi) \left[-(1 + ikR(\varphi))e^{-ikR(\varphi)} + 1 \right]}{R^3(\varphi)} d\varphi \\ &+ \partial_{r'} \mathcal{G} \end{aligned} \quad (C11)$$

and

$$\begin{aligned} \partial_{z'} \mathcal{G}_k &= \frac{1}{4\pi} \int_0^{2\pi} \frac{(z - z') \cos(\varphi) \left[(1 + ikR(\varphi))e^{-ikR(\varphi)} - 1 \right]}{R^3(\varphi)} d\varphi \\ &+ \partial_{z'} \mathcal{G} \end{aligned} \quad (C12)$$

The static terms on the right-hand sides of equations (C11) and (C12), defined in (C3) and (C4), can be treated using the same regularization procedure. In the limit $r \rightarrow 0$, the asymptotic behavior follows directly from the Bessel function representation in (C9):

$$\mathcal{G}_k(0, z; r', z') = 0, \quad \partial_{r'} \mathcal{G}_k(0, z; r', z') = 0, \quad \partial_{z'} \mathcal{G}_k(0, z; r', z') = 0.$$

When $r' = 0$, we have $\mathcal{G}_k(r, z; 0, z') = 0$, $\partial_{z'} \mathcal{G}_k(r, z; 0, z') = 0$, and

$$\begin{aligned} \partial_{r'} \mathcal{G}_k(r, z; 0, z') &= \frac{1}{4} \int_0^\infty J_1(\lambda r) \frac{\lambda^2}{\sqrt{\lambda^2 - k^2}} e^{-\sqrt{\lambda^2 - k^2}|z-z'|} d\lambda \\ &= \frac{r}{4\chi^3} (1 + ik\chi) e^{-ik\chi} \end{aligned} \quad (C13)$$

References

- [1] J. García-Martín, J. Gómez-Gil, E. Vázquez-Sánchez, Non-destructive techniques based on eddy current testing, *Sensors* 11 (3) (2011) 2525–2565.
- [2] N. Bowler, *Eddy-Current Nondestructive Evaluation*, Springer Series in Measurement Science and Technology, Springer, New York, 2019.

- [3] A. A. Bakr, The Boundary Integral Equation Method in Axisymmetric Stress Analysis Problems, Vol. 14 of Lecture Notes in Engineering, Springer-Verlag, Berlin, Heidelberg, 1986.
- [4] M. Tsuchimoto, K. Miya, T. Honma, H. Igarashi, Fundamental solutions of the axisymmetric Helmholtz-type equations, *Applied Mathematical Modelling* 14 (1990) 605–611.
- [5] A. H.-D. Cheng, Y. Abousleiman, T. Badmus, A Laplace transform BEM for axisymmetric diffusion utilizing pre-tabulated Green's Function, *Engineering Analysis with Boundary Elements* 9 (1) (1992) 39–46.
- [6] J. Priede, G. Gerbeth, Boundary-integral method for calculating poloidal axisymmetric AC magnetic fields, *IEEE Transactions on Magnetics* 42 (2) (2006) 301–308.
- [7] T. W. Dawson, On the singularity of the axially symmetric Helmholtz green's function, with application to BEM, *Applied Mathematical Modelling* 19 (10) (1995) 590–600.
- [8] O. Steinbach, Numerical Approximation Methods for Elliptic Boundary Value Problems: Finite and Boundary Elements, Springer, New York, 2008.
- [9] J. A. Stratton, L. J. Chu, Diffraction theory of electromagnetic waves, *Physical Review* 56 (1) (1939) 99–107.
- [10] G. B. Folland, Real Analysis: Modern Techniques and Their Applications, 2nd Edition, Wiley, New York, 1999.
- [11] B. A. Auld, J. C. Moulder, Review of advances in quantitative eddy current nondestructive evaluation, *Journal of Nondestructive Evaluation* 18 (1) (1999) 3–36.
- [12] M. Guiggiani, The evaluation of Cauchy principal value integrals in the boundary element method – a review, *Mathematical and Computer Modelling* 15 (3–5) (1991) 175–184.
- [13] S. A. Sauter, C. Schwab, Boundary Element Methods, Vol. 39 of Springer Series in Computational Mathematics, Springer, Berlin, Heidelberg, 2011.

- [14] S. A. Sauter, C. Schwab, Quadrature for hp -Galerkin BEM in \mathbb{R}^3 , Numerische Mathematik 78 (1997) 211–258.
- [15] M. G. Duffy, Quadrature over a pyramid or cube of integrands with a singularity at a vertex, SIAM Journal on Numerical Analysis 19 (6) (1982) 1260–1262.
- [16] C. Schwab, W. L. Wendland, On numerical cubatures of singular surface integrals in boundary element methods, Numerische Mathematik 62 (3) (1992) 343–369.
- [17] Y. Luo, X. Yang, Impedance variation in a coaxial coil encircling a metal tube adapter, Sensors 23 (19) (2023) 8302.
- [18] G. Szegő, Orthogonal Polynomials, 4th Edition, Vol. 23 of American Mathematical Society Colloquium Publications, American Mathematical Society, Providence, RI, 1975.
- [19] J. T. Conway, Exact solutions for the magnetic fields of axisymmetric solenoids and current distributions, IEEE Transactions on Magnetics 37 (4) (2001) 2977–2988.
- [20] A. Sommerfeld, Vorlesungen über Theoretische Physik. Band VI: Partielle Differentialgleichungen der Physik, Verlag Harri Deutsch, Frankfurt am Main / Thun, 1978.
- [21] G. N. Watson, A Treatise on the Theory of Bessel Functions, 2nd Edition, Cambridge University Press, Cambridge, 1944.